Journal of Materials Chemistry A

ROYAL SOCIETY OF CHEMISTRY

PAPER

View Article Online
View Journal | View Issue

Cite this: J. Mater. Chem. A, 2026, 14, 15859

Size-tunable Zn_2SnO_4 octahedra possessing two lattice phases for the thiol–ene reaction

Yu-Shun Su,[a] Bo-Hao Chen [ab] and Michael H. Huang *[a]

Received 27th November 2025
Accepted 2nd March 2026

DOI: 10.1039/d5ta09685e

rsc.li/materials-a

By adjusting the volume of LiOH used, octahedral Zn_2SnO_4 particles with average sizes of 285 nm, 655 nm, and 1.5 μm have been synthesized hydrothermally. Observation of several additional X-ray diffraction (XRD) peaks suggests the presence of a trigonal phase instead of the normal cubic phase of Zn_2SnO_4. Synchrotron XRD analysis verifies that the 655 nm and 1.5 μm octahedra possess a trigonal phase with bulk and surface layer lattices differing by slight cell constant changes, while the 285 nm octahedra are better fitted with a trigonal bulk lattice and a cubic phase in the thick surface layer. High-resolution transmission electron microscopy (HR-TEM) characterization also reveals distinct lattice point differences in the crystal bulk and surface layer. These structural features should be important for their significant band gap shifts despite the large particle dimensions. Attributed to better light absorption, the 1.5 μm octahedra showed the best dye photodegradation activity. They also exhibited the best efficiency in the thiol–ene reaction to couple thiolphenol and styrene to generate thioether. The particle size- and shape-related lattice variations are broadly present in semiconductor crystals to affect their various properties.

Introduction

Diverse properties of semiconductor crystals display facet dependence, including electrical conductivity, photocatalytic activity, light absorption, piezoelectricity, dielectric constant, piezocatalytic activity, electrocatalytic activity, and magnetism.[1–12] The emergence of all these phenomena arises from the presence of a facet-specific surface layer within the crystals with lattice distortions, as well as lattice constant changes in the interior bulk, as revealed by synchrotron XRD pattern analysis and fast Fourier transform of HR-TEM images.[5–9,11,13] In addition to facet effect observations, crystals having the same shape but different sizes also exhibit slight lattice constant changes. Previously, Ag_2O, Fe_3O_4 and MnS polyhedra have revealed size-dependent lattice constant changes.[5,11,14] Because of the lattice variations among crystals of tunable sizes and shapes, they absorb light of somewhat different wavelengths and have dissimilar band gaps. To explore more examples of how interior lattice alteration can tune optical and photocatalytic properties, Zn_2SnO_4 is an interesting choice, as zinc stannate cuboctahedra and truncated octahedra have been found to exhibit dual lattice phases, with a major cubic $Fd\bar{3}m$ inverse spinel phase and a minor $R\bar{3}m$ phase, which is a subgroup of $Fd\bar{3}m$ with a lower symmetry.[15] In this zinc tin oxide, O^{2-} ions occupy the face-centered cubic sites, Zn^{2+} ions fully reside in the tetrahedral sites, while Zn^{2+} and Sn^{4+} ions equally share the octahedral sites.[16] Zn_2SnO_4 possesses a direct band gap of 3.7 eV.[16,17] It has been used as an anode material for lithium ion batteries.[18,19] Gas sensing and solar cell applications have been examined.[20] Zn_2SnO_4 crystals were generally produced by hydrothermally heating a mixture of chemicals containing zinc and tin ions and a base. While Zn_2SnO_4 octahedra composed of plate-like structures on the surface have been observed, octahedra with smooth surfaces were also obtained.[21,22] Microcubes were also reported.[23]

In addition to photocatalytic dye degradation and hydrogen evolution reactions, semiconductor crystals can also photocatalyze organic transformations using the photogenerated electrons, holes and radicals.[2,6,24,25] We consider employing Zn_2SnO_4 crystals for the photocatalytic thiol–ene click reaction to generate thioethers. Thioethers are an important class of organosulfur compounds that are widely found in natural products and pharmaceuticals and are precursors for the preparation of sulfoxides and sulfones.[26,27] A ruthenium complex has been applied for photocatalytic anti-Markovnikov hydrothiolation of olefins.[28] Uncharacterized TiO_2 also can photocatalyze the thiol–ene reaction in 16 to 40 h.[29] The reaction can also be accomplished using $ZnIn_2S_4$ microcrystals in 15 h with moderate yields.[30] It would be desirable to perform the reaction using a Zn_2SnO_4 photocatalyst.

In this study, Zn_2SnO_4 octahedra with tunable sizes have been synthesized hydrothermally. In-house XRD patterns suggest the presence of a different phase other than the normal cubic lattice. Synchrotron XRD analysis and crystal structure modeling yield bulk and surface lattices that are best fitted with the trigonal $R\bar{3}m$ space group for larger octahedra, while the

[a]Department of Chemistry, National Tsing Hua University, Hsinchu, 300044, Taiwan. E-mail: hyhuang@mx.nthu.edu.tw
[b]National Synchrotron Radiation Research Center, Hsinchu, 300092, Taiwan

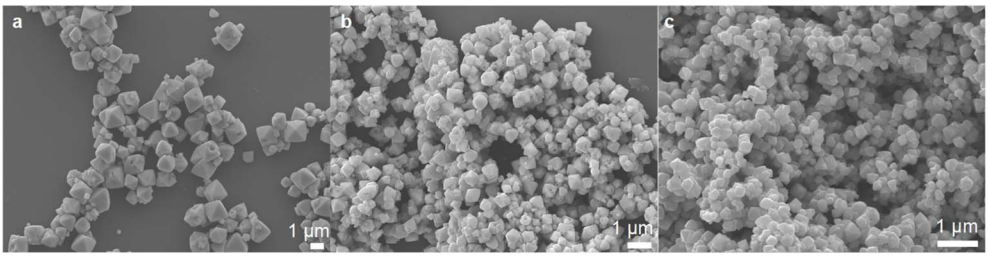

Fig. 1 SEM images of the synthesized $ZnSnO_4$ octahedra with average opposite corner lengths of (a) 1.5 μm, (b) 655 nm, and (c) 285 nm.

smallest octahedra are better fitted with a combination of $R\bar{3}m$ and cubic $Fd\bar{3}m$ space groups. HR-TEM processing directly enables visualization of the surface layer lattice. Optical properties were examined. The largest 1.5 μm octahedra possess the best photocatalytic dye degradation activity. They also are the best photocatalyst for the thiol–ene reaction. Active species trapping experiments have been performed to support the proposed reaction mechanism.

Results and discussion

Synthesis and characterization of Zn_2SnO_4 octahedra

By adjusting the concentration of LiOH, Zn_2SnO_4 octahedra with opposite corner lengths of 285 nm, 655 nm, and 1.5 μm were obtained hydrothermally at 180 °C for 9 h. Fig. 1 presents scanning electron microscopy (SEM) images of the synthesized particles, showing generally good size and shape uniformity. Their size distribution histograms are available in Fig. S1, SI. The in-house XRD patterns of Zn_2SnO_4 octahedra with different sizes are shown in Fig. 2. The diffraction patterns match well with that of the cubic phase of Zn_2SnO_4 with a $Fd\bar{3}m$ space group. As the particle size increases, a slight shift of the peaks toward lower angles can be identified. However, subtle peak splitting is noticeable at 35.2° and 60.2°, suggesting the presence of another crystal phase.

To confirm the peak shift and splitting features, synchrotron XRD data were collected. These data were subsequently employed to determine the crystal space group through Rietveld refinement. Fig. S2, SI gives selected synchrotron XRD peaks. Clearly, an additional peak is observed next to the (222) and (422) peaks, and the (440) peak appears asymmetric, likely from an overlap of two peaks. This observation is consistent with that in a previous report that this sample contains the $R\bar{3}m$ space group.[15] Since there is no reference standard for Zn_2SnO_4 in the $R\bar{3}m$ space group, the synchrotron-derived diffraction patterns were analyzed using the direct method in Expo2014 software. As depicted in Fig. 3, the cubic $Fd\bar{3}m$ phase and trigonal $R\bar{3}m$ phase are structurally similar, especially when viewed along the [110] direction for the $Fd\bar{3}m$ structure. The observed diffraction intensities together with the model phase information were

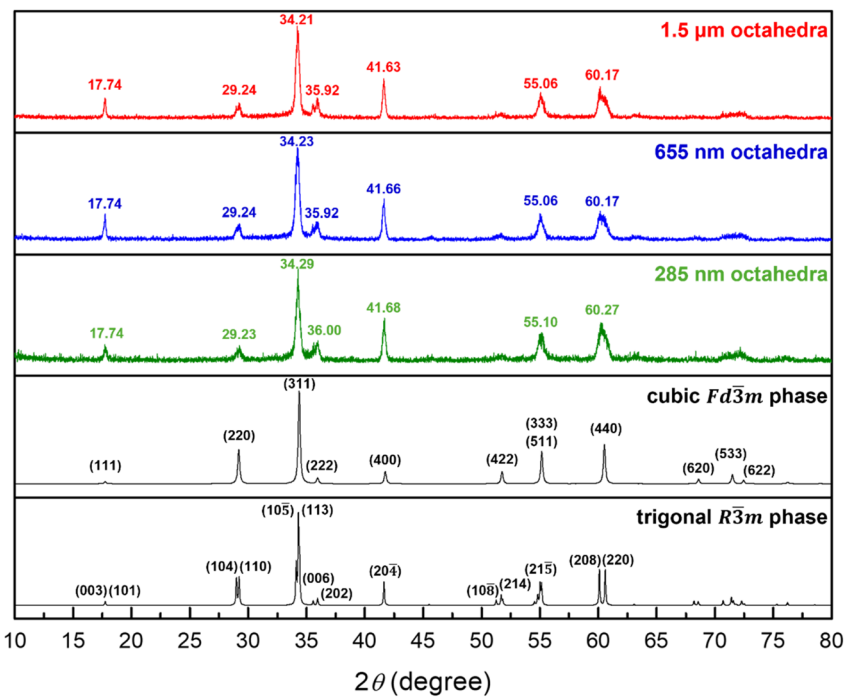

Fig. 2 XRD patterns of the size-tunable Zn_2SnO_4 octahedra. Reference cubic and calculated trigonal phases of Zn_2SnO_4 are also shown.

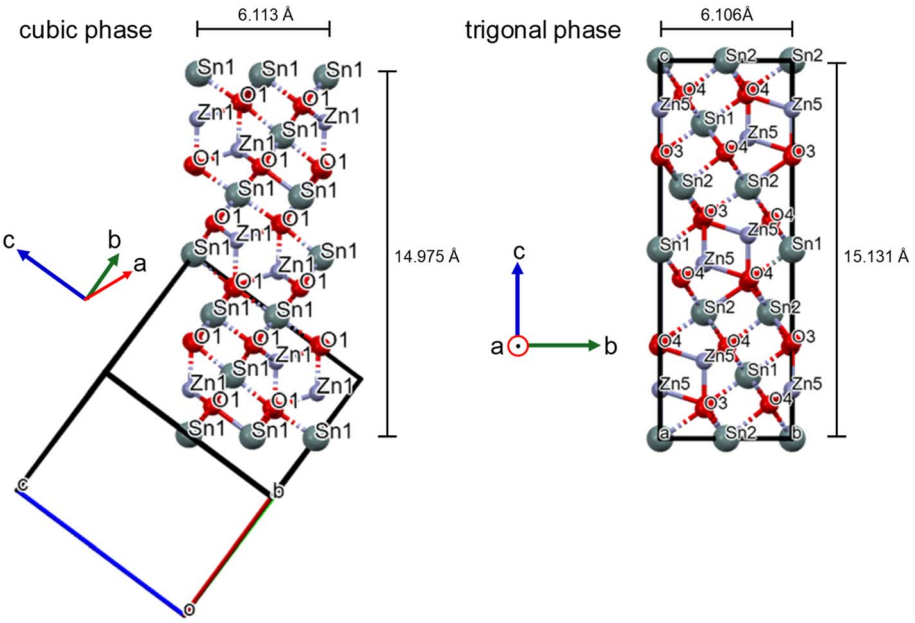

Fig. 3 Crystal structures of the cubic $Fd\bar{3}m$ phase viewed along the [110] direction and the trigonal $R\bar{3}m$ phase.

used to calculate the three-dimensional electron density distribution. The atomic positions (Q1, Q2, …) were then assigned by comparing their relative positions with those in the $Fd\bar{3}m$ cubic phase. During the space group transformation, position splitting occurs due to a reduction in symmetry. The number of atomic positions increases upon converting from the cubic to the trigonal phase, as shown in Table S1, SI. Zn1 transforms into Zn5, Zn2 into Zn6 and Zn7, Sn1 into Sn1 and Sn2, and O1 into O3 and O4. Fig. 2 also presents the calculated XRD pattern of the $R\bar{3}m$ phase, showing the emergence of additional peaks.

Fig. S3 and Table S2, SI provide Rietveld refinement results for the three Zn_2SnO_4 particle sizes. A zero-point shift correction was applied to account for human error caused in sample placement. It was found that 655 nm and 1.5 μm octahedra can be best fitted using two $R\bar{3}m$ phases to represent the bulk and

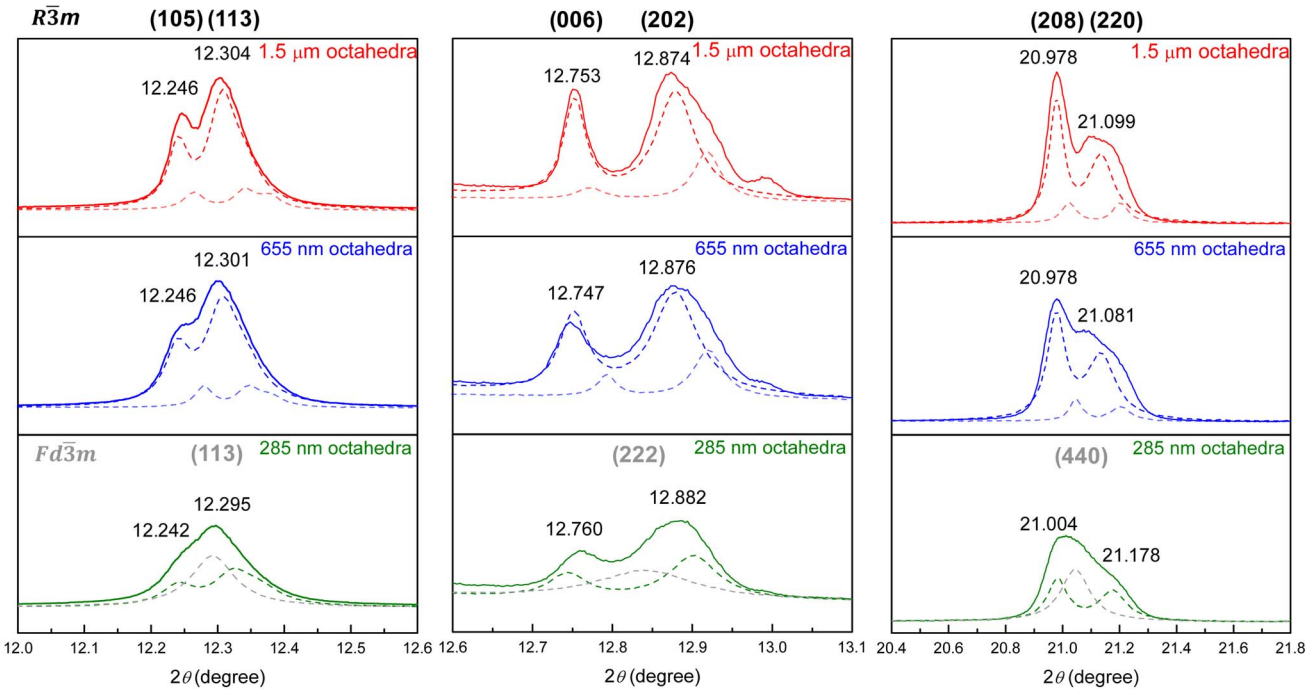

Fig. 4 Enlarged synchrotron XRD patterns of the size-tunable Zn_2SnO_4 octahedra, highlighting the bulk and surface $R\bar{3}m$ lattices of 655 nm and 1.5 μm octahedra, and the bulk $R\bar{3}m$ lattice and surface $Fd\bar{3}m$ lattice of 285 nm octahedra.

surface layer lattices. The 285 nm octahedra are closer to the cubic phase but still exhibit peak splitting, so they can be described to possess both cubic and trigonal phases. On the basis of microstrain values, as seen in Table S2, SI, the cubic $Fd\bar{3}m$ phase with an overall larger microstrain is designated to appear near the particle shell region, since the surface experiences greater tensile stress. The interior bulk is considered to possess the trigonal $R\bar{3}m$ phase. On the basis of deconvoluted XRD peak areas of the 285 nm octahedra, the shell region accounts for 43.4 weight%. Fig. 4 gives the selected peaks in synchrotron XRD patterns of the Zn_2SnO_4 octahedra, showing the peak profiles can be fitted with bulk and surface layer lattices with slight cell constant changes for larger octahedra, and two different crystal phases for the 285 nm octahedra.

In addition to the analysis of the unit cell and μ strain, the atomic positions were also calculated, since Zn and O atoms are mobile in the trigonal phase. Variations in interatomic distances within the unit cell are summarized in Table S3, SI. As illustrated in Fig. S4, SI, the positions of Zn5, O3, and O4 exhibit some changes between the bulk and surface. Bond length variations are depicted in Fig. S5, SI. Comparing the bulk and surface lattices of the same particle size, the Zn5–O distances in the bulk lattice are significantly elongated. As a result, Zn5 coordination deviates from an ideal tetrahedral geometry and becomes an elongated tetrahedron along the *c*-axis. For the Sn1–O4 octahedron, although all Sn–O bond lengths remain equivalent, they are considerably shortened to 1.58 Å in the bulk lattice, which is much smaller than the typical Sn–O bond length of about 2.2 Å. In the case of Sn2–O, the displacement of O3 leads to a distorted octahedron. In contrast, the degree of distortion in the surface layer lattices of 655 nm and 1.5 μm octahedra is relatively minor, and the local chemical environments around Zn and Sn largely preserve the ideal Zn–O tetrahedral and Sn–O octahedral configurations. Notably, the 1.5 μm octahedra display the largest octahedral distortion.

Fig. 5 provides TEM characterization of a 285 nm Zn_2SnO_4 octahedron. The HR-TEM image reveals distinct lattice fringes. The measured lattice spacing between two adjacent fringes is 5.36 Å, which corresponds to the (111) planes of the cubic phase. The selected-area electron diffraction (SAED) pattern, taken along the [011] zone axis, displays well-defined diffraction spots, indicating that the synthesized Zn_2SnO_4 octahedra are single-crystalline. More importantly, fast Fourier transform (FFT) of the HR-TEM image reveals that while lattice spots in the

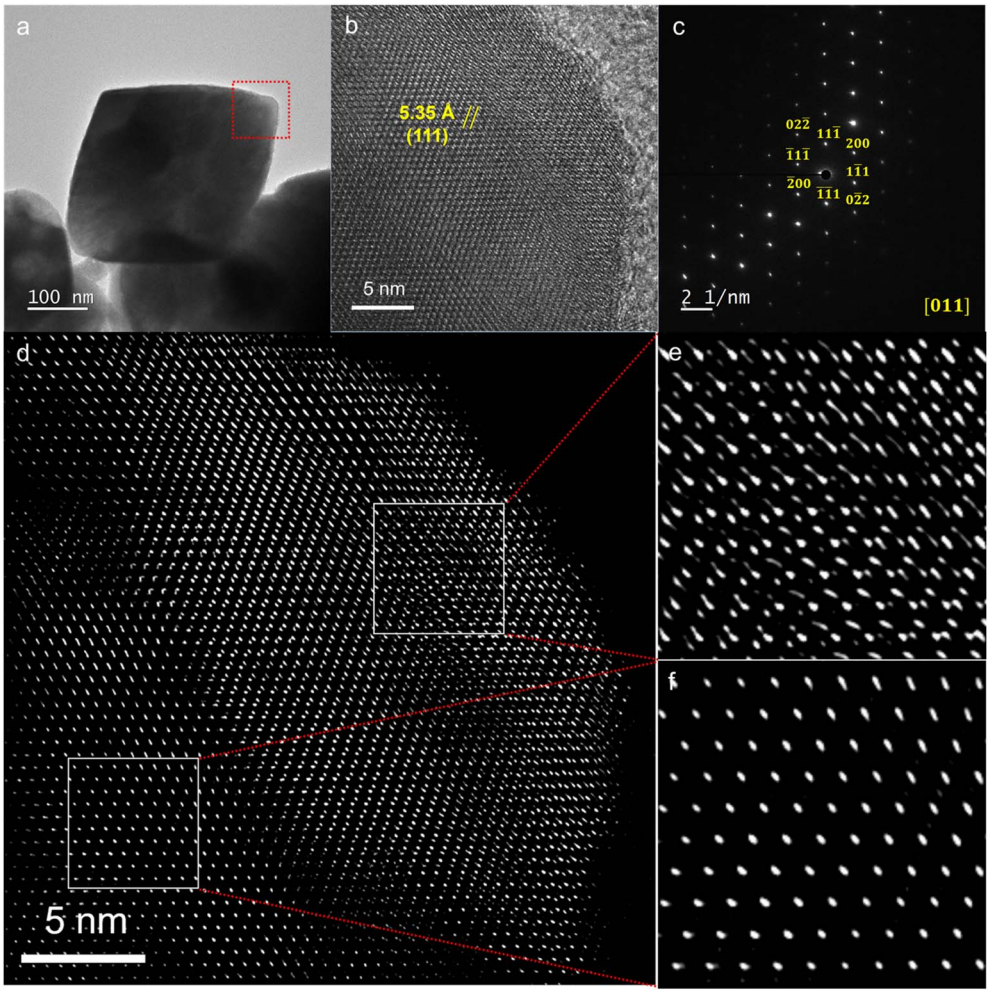

Fig. 5 (a) TEM image of a Zn_2SnO_4 octahedral particle oriented along the [110] direction. (b and c) HR-TEM image of the red frame region in panel (a) and its SAED pattern. (d–f) FFT-processed lattice spot image of panel (b) and the expanded views of the two square regions.

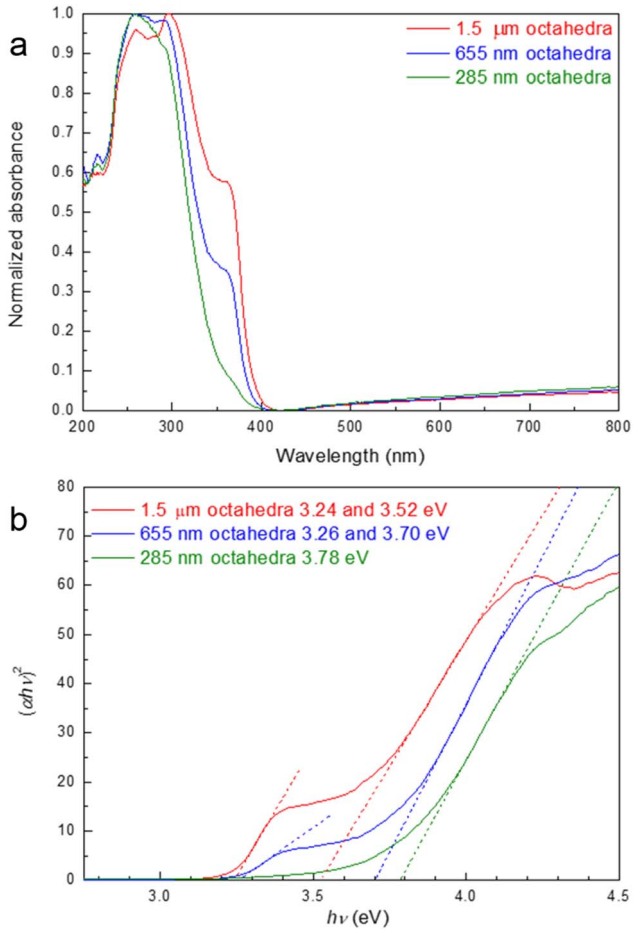

Fig. 6 (a) Diffuse reflectance spectra of the size-tunable Zn_2SnO_4 octahedra and (b) the corresponding Tauc plot.

interior region show some positional deviation, lattice spots in the surface layer region are significantly elongated. There are apparently more than one set of lattice points in the region closer to the crystal surface, also showing some degree of positional deviation. The surface layer is quite thick, which is consistent with synchrotron XRD analysis. This examination visually proves the co-existence of two crystal phases in the surface layer region.

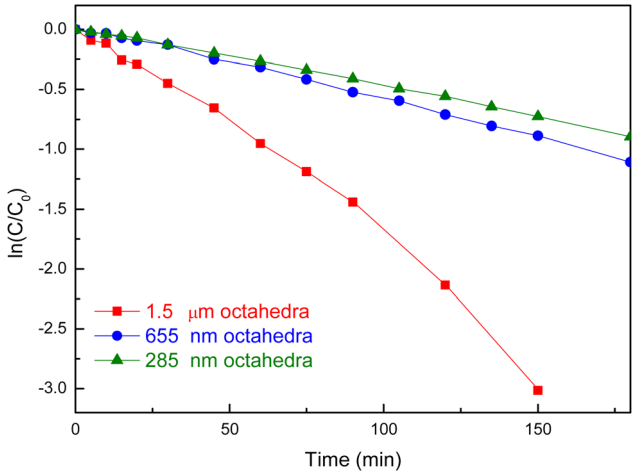

Fig. 7 Extents of methylene blue degradation with irradiation time for different Zn_2SnO_4 samples.

Table 1 Synthesis of 2-phenylethyl phenyl sulfide photocatalyzed by Zn_2SnO_4 octahedra[a]

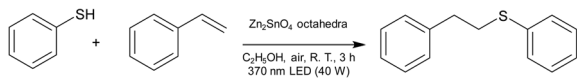

Entry	Catalyst	Amount (mg)	NMR yield (%)
1	1.5 μm octahedra	5	95
2	655 nm octahedra	2.4	88
3	285 nm octahedra	1	88
4	No catalyst	—	75

[a] Reagents: thiolphenol (1.2 mmol), styrene (1 mmol), C_2H_5OH (3 mL). Triphenylmethane is used as the internal standard.

Fig. 6 shows diffuse reflectance spectra of the Zn_2SnO_4 octahedra and the corresponding Tauc plot. With increasing particle size, the absorption edge becomes red-shifted, as expected. However, the absorption shifts are exceptionally large at these dimensions, demonstrating that the optical size effect can really extend to very large particles.[32] Interestingly, for 655 nm and 1.5 μm octahedra, there is an additional absorption band at around 370 nm. Such an optical feature has appeared in the Zn_2SnO_4 literature.[15,31] Consequently, these two samples show two band gaps, with the normal band gaps of 3.52 and 3.70 eV for the 1.5 μm and 655 nm octahedra, respective, and 3.24 and 3.26 eV coming from the shoulder band absorption. It is unclear if the shoulder band appears from the substantial shell lattice. For 285 nm octahedra, a larger band gap of 3.78 eV was

Table 2 Substrate scope for sulfide formation[a]

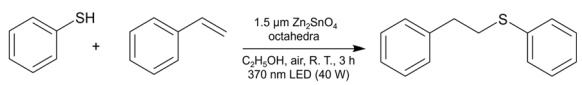

Entry	Arylthiol	Product	NMR yield (%)
1	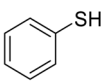	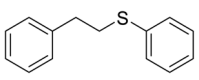	95
2	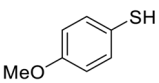	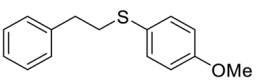	72
3	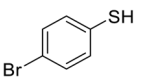	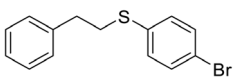	80
4	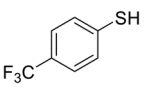	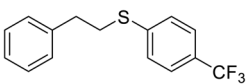	80

[a] Reagents: arylthiol (1.2 mmol), styrene (1 mmol), Zn_2SnO_4 (5 mg), C_2H_5OH (3 mL).

Table 3 Active species scavenging experiments[a]

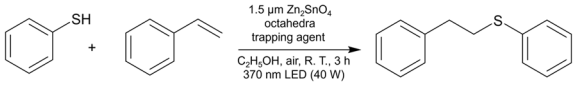

Entry	Trapping agent	NMR yield (%)
1	$KBrO_3$ (e^-)	84
2	DIPEA (h^+)	42
3	*iso*-Propanol ($^{\bullet}OH$)	90
4	DABCO ($^1O_2$)	56
5	1,4-Benzoquinone ($O_2^{\bullet-}$)	23

[a] Reagent: thiolphenol (1.2 mmol), styrene (1 mmol), Zn_2SnO_4 (5 mg), trapping agent (1 mmol), C_2H_5OH (3 mL).

obtained. Thus, the band gap difference between the 285 nm and 1.5 μm octahedra is 0.54 eV.

Photocatalytic reactions

The size-tunable Zn_2SnO_4 octahedra were first compared for photocatalytic dye degradation under 370 nm LED lamp irradiation. Different amounts of particles for these samples were used to keep the total particle surface area constant. Fig. S6, SI shows UV-vis absorption spectra of methylene blue as a function of irradiation time on these octahedra. Fig. 7 summarizes the photodegradation results. Unexpectedly, the largest 1.5 μm octahedra exhibited the best degradation efficiency with the highest rate constant ($k = 0.016\ s^{-1}$). The 285 nm and 655 nm octahedra have similarly lower degradation activities. This happens presumably because the 1.5 μm octahedron sample has the highest light absorption around 370 nm to generate more photoexcited electrons and holes.

Zn_2SnO_4 likely has not been explored as a photocatalyst for organic synthesis. The size-tunable Zn_2SnO_4 octahedra were employed to photocatalyze the coupling of thiolphenol and styrene to generate 2-phenylethyl phenyl sulfide. Table 1 lists the product yields after 3 h under 370 nm LED lamp irradiation, using octahedra of different sizes but with a fixed total surface area. The 1.5 μm octahedra achieved a high product yield of 95%, while the 655 nm and 285 nm octahedra both delivered yields of 88%. However, in the absence of any photocatalyst, the reaction can still occur with a good yield of 75%. This shows that another reaction mechanism is operative. Nevertheless, it is beneficial to use the surface-controlled octahedra to enhance the reaction yield. Fig. S7, SI shows a SEM image of Zn_2SnO_4 octahedra after the thiol–ene reaction. The particle morphology appears largely maintained, although some degree of particle agglomeration is observed. The 1.5 μm octahedra were subsequently employed for the thiol–ene reaction using thiophenols bearing different substituents under identical reaction conditions. Table 2 lists the substrate scope results. The yields of (4-methoxyphenyl)(phenethyl)sulfane, (4-bromophenyl)(phenethyl)sulfane, and phenethyl(4-(trifluoromethyl)phenyl)sulfane were 72%, 80%, and 80%, respectively, indicating that substrates containing either electron-donating or electron-withdrawing groups can afford satisfactory yields.

To probe the reaction mechanism, various trapping agents were added in the thiol–ene reaction (Table 3). First, in the presence of $KBrO_3$ acting as an electron scavenger, a modest decrease in yield to 84% was obtained. Introduction of *N*,*N*-diisopropylethylamine (DIPEA) as a hole scavenger led to a significant drop in product yield to 42%, indicating that the photogenerated holes are critically involved in the reaction. Since the same amount of electron and hole scavengers was used, electron transfer to the solution species can still be significant. Subsequently, *iso*-propanol was used as a hydroxyl radical scavenger. The product yield was 90%, inferring that hydroxyl radicals are not the active species in this reaction. Next, 1,4-diazabicyclo[2,2,2]octane (DABCO) and 1,4-benzoquinone were introduced as scavengers for superoxide radicals and singlet oxygen, respectively. The yields dropped sharply to 56% and 23%, demonstrating that superoxide radicals and singlet oxygen are active species in the coupling reaction.

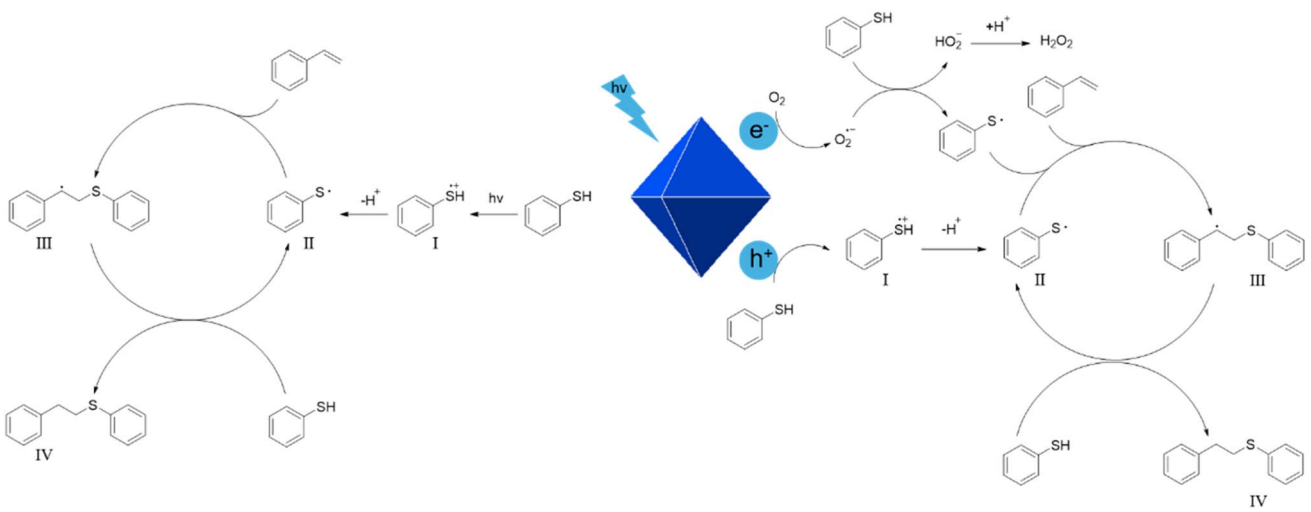

Fig. 8 Proposed mechanisms of thiol–ene reaction photocatalyzed by Zn_2SnO_4 octahedra.

To further investigate the reaction mechanism, electron paramagnetic resonance (EPR) analysis was conducted. Due to the short lifetime of free radicals, 5,5-dimethyl-1-pyrroline *N*-oxide (DMPO) was employed as a spin-trapping reagent to capture radicals and form stable adducts. DMPO reacts with superoxide radicals to form a DMPO–OOH adduct, which produces a characteristic eight-line pattern in the EPR spectrum. In contrast, formation of a DMPO–OH adduct from the release of hydroxyl radicals is characterized by a four-line pattern.[33] Fig. S8, SI shows the EPR spectrum of DMPO upon 370 nm light irradiation on Zn_2SnO_4 octahedra in methanol. The signal matches well with that of the DMPO–OOH adduct, indicating that superoxide radicals are a major reactive species generated by Zn_2SnO_4 under UV light irradiation.

Based on the results of the scavenging experiments and EPR data, a possible mechanism for the photocatalytic thiol–ene reaction is proposed (Fig. 8).[2,30] Upon UV irradiation on Zn_2SnO_4 octahedra, photoexcited electrons and holes are formed. The holes react with thiol molecules to produce thiyl radical cations (intermediate I), which then undergo deprotonation to form thiyl radicals (intermediate II). Meanwhile, the photoexcited electrons in the conduction band reduce O_2 to form superoxide radicals. Superoxide radicals react with thiol molecules to generate thiyl radicals along with hydroperoxide anions (HO_2^-). The unstable HO_2^- further reacts with protons to produce hydrogen peroxide. The reactive thiyl radicals then add to the C=C double bond of styrene, generating alkyl radicals (intermediate III), which abstract protons from unreacted thiol molecules to yield the final products (IV), while regenerating thiyl radicals to propagate the radical reaction. Alternatively, thiophenol itself can directly form thiyl radicals under UV irradiation. This explains why the reaction can still occur in the absence of a photocatalyst.

Conclusions

Large Zn_2SnO_4 octahedra with three average sizes ranging from 285 nm to 1.5 μm have been synthesized. In addition to the observation of peak splitting in in-house XRD patterns to suggest the presence of a new trigonal $R\bar{3}m$ phase, synchrotron XRD measurements revealed the possession of both the cubic and trigonal phases for the smallest octahedra, with a trigonal-phased bulk and a cubic-phased surface layer. For larger octahedra, the trigonal phase forms the bulk and surface layer lattices with slight cell constant changes. HR-TEM analysis reveals distinction between bulk and surface layer lattices. Despite the large particle dimensions, significant band gap shifts from 3.78 eV to 3.52 eV were observed with increasing particle size. The 1.5 μm octahedra outperformed 655 and 285 nm octahedra in photocatalytic dye degradation. The Zn_2SnO_4 octahedra can also enhance the photochemical coupling between thiophenol and styrene. Lattice variations continue to be observable in diverse semiconductor crystals to affect their properties.

Experimental

Chemicals

Tin tetrachloride ($SnCl_4$, 99%, NOVA), zinc sulfate heptahydrate ($ZnSO_4 \cdot 7H_2O$, 99.5%, SHOWA), lithium hydroxide monohydrate ($LiOH \cdot H_2O$, 98%, Thermo Scientific), sodium hydroxide (NaOH, >98%, Honeywell), diethylene glycol ($C_4H_{10}O_3$, 99%, Thermo Scientific), acetic acid (CH_3COOH, 99.8%, Honeywell), ethanol (C_2H_5OH, 99.8%, Honeywell), thiophenol (C_6H_6S, 99+%, Thermo Scientific), styrene (C_8H_8, 99%, Alfa Aesar), 4-methoxythiophenol (C_7H_8OS, 98%, NOVA), 4-bromothiophenol (C_6H_5SBr, 98%, NOVA), 4-(trifluoromethyl) benzenethiol ($C_7H_5F_3S$, 97%, NOVA), triphenylmethane ($(C_6H_5)_3CH$, 98% NOVA), *iso*-propanol (C_3H_8O, 99.5%, Sigma-Aldrich), 1,4-diazabicyclo[2.2.2]octane (DABCO, $C_6H_{12}N_2$, 98%, Alfa Aesar), 1,4-benzoquinone ($C_6H_4O_2$, 98%, Alfa Aesar), potassium bromate ($KBrO_3$, 99%, Alfa Aesar), *N*,*N*-diisopropylethylamine (DIPEA, $C_8H_{19}N$, 99.5%, Acros Organics), and 5,5-dimethyl-1-pyrroline *N*-oxide (DMPO, $C_6H_{11}NO$, 98%, Matrix Scientific) were used as received.

Synthesis of size-tunable Zn_2SnO_4 octahedra

Using the synthesis of 1.5 μm Zn_2SnO_4 octahedra as an example, 0.029 mL (0.25 mmol) of $SnCl_4$ was first added into a vial containing 5.5 mL of deionized water and stirred for 5 min. Then, 1 mL of 0.5 M $ZnSO_4$ solution was added and stirred for another 5 min, maintaining a molar ratio of Sn : Zn = 1 : 2. Subsequently, 3.5 mL of 0.8 M LiOH was slowly added dropwise. To prepare 655 and 285 nm octahedra, the volumes of LiOH solution was increased to 4 and 4.5 mL, while the added water volumes were 5 and 4.5 mL, respectively. See Table S4, SI for the complete reagent amounts used. The mixture was stirred for 30 min and then transferred to a 25 mL Teflon-lined autoclave, which was heated in an oven at 180 °C for 9 h. After cooling to room temperature, the resulting white precipitate was collected by centrifugation at 11 000 rpm for 4 min. The product was then washed in 10 mL of 5% acetic acid under ultrasonic treatment for 30 min to remove any ZnO impurity. Further washing was carried out several times using deionized water and ethanol, and the final product was stored in ethanol.

Photocatalytic dye degradation

To compare the photocatalytic dye degradation activities of Zn_2SnO_4 octahedra with different particle sizes, the required weight of each catalyst was calculated to ensure an equal surface area. The calculated amounts are listed in Table S5, SI. A measured amount of Zn_2SnO_4 octahedra was first placed into a 4 cm × 4 cm × 4 cm quartz cell, followed by the addition of 4.5 mL of 100 ppm methylene blue solution. Deionized water was then added to reach a total volume of 45 mL. The quartz cell was positioned 2 cm away from the light source and stirred in the dark for 30 min to achieve adsorption–desorption equilibrium. A 40 W blue LED lamp ($\lambda = 370$ nm) was used as the light source. The measured light intensity reaching the sample was 0.73 W cm^{-2}. At specific time intervals, 1 mL of the suspension was withdrawn, centrifuged, and the absorbance of the supernatant was measured.

Photocatalytic 2-phenylethyl phenyl sulfide formation

First, Zn_2SnO_4 octahedra with the same total particle surface area were weighed and placed into a 15 mL oven-dried quartz

tube. A mixture of 0.122 mL (1.2 mmol) of thiophenol, 0.114 mL (1 mmol) of styrene, and 3 mL of ethanol was prepared and added into the quartz tube. The tube was then sealed with a serum stopper, sonicated for 1 min, and placed 2 cm away from the light source. A fan was turned on to remove hot air around the quartz tube from light illumination. The reaction was carried out under stirring at room temperature under a 40 W blue LED lamp ($\lambda = 370$ nm) for 3 h. After the reaction, the mixture was transferred to a 15 mL centrifuge tube and centrifuged at 11 000 rpm for 4 min to separate the catalyst. The supernatant was collected and concentrated using a rotary evaporator under vacuum. Finally, 1 mmol of triphenylmethane was added as an internal standard to the product, and the yield was determined by nuclear magnetic resonance (NMR) spectroscopy.

Instrumentation

The morphology of Zn_2SnO_4 particles were characterized using a JEOL JSM-7000F scanning electron microscope. The particle crystalline structure was examined using a JEOL JEM-ARM200FTH high-resolution transmission electron microscope. The in-house X-ray diffraction data were obtained using a powder X-ray diffractometer (Rigaku SmartLab 40 kV, 50 mA) with Cu Kα radiation. The high-resolution powder X-ray diffraction data were collected using the Taiwan Photon Source 19A beamline (TPS19A) in NSRRC with a wavelength of 0.56025 Å (X-ray energy of 22.13 keV). UV-vis absorption spectra were obtained using a JASCO V-670 spectrometer with a solid sample holder attached. A Bruker ELEXSYSE 580 CW/Pulse spectrometer was used to obtain EPR spectra. ^{1}H nuclear magnetic resonance (NMR) spectra were obtained with the use of a Bruker Avance II 400 MHz NMR spectrometer.

Conflicts of interest

There are no conflicts to declare.

Data availability

All the data have been presented in the manuscript and its supplementary information (SI). Supplementary information is available. See DOI: https://doi.org/10.1039/d5ta09685e.

Acknowledgements

Financial support was provided by the National Science and Technology Council, Taiwan (NSTC 112-2113-M-007-016-MY3). Ms Juo-Chi Chen of NTHU Instrumentation Center provided assistance in the EPR measurements, Ms Swee-Lan Cheah assisted in the XPS analysis, and Mr Yung-Sheng Chen assisted in the HR-TEM characterization.

References

1 V. Meena and M. H. Huang, *Nanoscale*, 2025, **17**, 22414–22421.
2 W.-T. Dai, C.-C. Wen, H.-J. Lin and M. H. Huang, *ACS Appl. Mater. Interfaces*, 2025, **17**, 18268–18274.
3 P.-J. Chou, W.-Y. Yu, J.-C. Kao, Y.-C. Lo, J.-P. Chou and M. H. Huang, *ACS Appl. Electron. Mater.*, 2025, **7**, 360–368.
4 W. Adamowicz, W. Macky and M. Kobielusz, *J. Mater. Chem. A*, 2025, **13**, 19623–19630.
5 P.-S. Chang, B.-H. Chen, Y.-C. Lin, W.-T. Dai, G. Kumar, Y.-G. Lin and M. H. Huang, *Small*, 2024, **20**, 2401558.
6 Y.-T. Yang, B.-H. Chen, A. Pal, C.-H. Li, Z.-H. Lin and M. H. Huang, *J. Mater. Chem. A*, 2025, **13**, 10475–10486.
7 Y.-J. Chuang, A. Pal, B.-H. Chen, S. Jena, S. Suresh, Z.-H. Lin and M. H. Huang, *Chem. Sci.*, 2025, **16**, 3285–3295.
8 B.-H. Chen, S. Jena, Y.-J. Chuang, H.-Y. Lin, C.-H. Li, J. M. Wu and M. H. Huang, *J. Phys. Chem. Lett.*, 2025, **16**, 4921–4926.
9 S. Jena, B.-H. Chen, H.-Y. Lin, V. Meena, W.-F. Chang, J. M. Wu and M. H. Huang, *ACS Appl. Nano Mater.*, 2025, **8**, 19549–19557.
10 G. Kumar, H.-W. Sun and M. H. Huang, *ACS Appl. Nano Mater.*, 2024, **7**, 2155–2163.
11 J.-H. Yang, C.-P. Wang, B.-H. Chen and M. H. Huang, *Inorg. Chem.*, 2025, **64**, 8659–8667.
12 C.-C. Chang, J.-C. Kao, Y.-C. Lo, J.-P. Chou, S.-C. Lin, C.-C. Wen and M. H. Huang, *J. Mater. Chem. A*, 2025, **13**, 13186–13194.
13 B.-H. Chen, G. Kumar, Y.-J. Wei, H.-H. Ma, J.-C. Kao, P.-J. Chou, Y.-C. Chuang, I.-C. Chen, J.-P. Chou, Y.-C. Lo and M. H. Huang, *Small*, 2023, **19**, 2303491.
14 C.-K. Chen, B.-H. Chen and M. H. Huang, *Chem. Mater.*, 2023, **35**, 7859–7866.
15 Y.-Q. Jiang, X.-X. Chen, R. Sun, Z. Xiong and L.-S. Zheng, *Mater. Chem. Phys.*, 2011, **129**, 53–61.
16 S. Baruah and J. Dutta, *Sci. Technol. Adv. Mater.*, 2011, **12**, 013004.
17 X. Fu, X. Wang, J. Long, Z. Ding, T. Yan, G. Zhang, Z. Zhang, H. Lin and X. Fu, *J. Solid State Chem.*, 2009, **182**, 517–524.
18 A. Rong, X. P. Gao, G. R. Li, T. Y. Yan, H. Y. Zhu, J. Q. Qu and D. Y. Song, *J. Phys. Chem. B*, 2006, **110**, 14754–14760.
19 X. Liu, C. Niu, J. Meng, X. Xu, X. Wang, B. Wen, R. Guo and L. Mai, *J. Mater. Chem. A*, 2016, **4**, 14095–14100.
20 S. Sun and S. Liang, *J. Mater. Chem. A*, 2017, **5**, 20534–20560.
21 Z. Li, Y. Zhou, J. Zhang, W. Tu, Q. Liu, T. Yu and Z. Zou, *Cryst. Growth Des.*, 2012, **12**, 1476–1481.
22 X. Ji, X. Huang, J. Liu, J. Jiang, X. Li, R. Ding, Y. Hu, F. Wu and Q. Li, *J. Alloys Compd.*, 2010, **503**, L21–L25.
23 Z. Ai, S. Lee, Y. Huang, W. Ho and L. Zhang, *J. Hazard. Mater.*, 2010, **179**, 141–150.
24 K.-C. Chien, W.-Y. Yu, J.-C. Kao, Y.-C. Lo, J.-P. Chou and M. H. Huang, *J. Mater. Chem. A*, 2024, **12**, 5429–5438.
25 G.-R. Wang and M. H. Huang, *J. Mater. Chem. A*, 2024, **12**, 13792–13799.
26 Q. Xiao, Q.-X. Tong and J.-J. Zhong, *Molecules*, 2022, **27**, 619.
27 M.-H. Hsieh, Z.-H. Su, E.-T. Wu and M. H. Huang, *ACS Appl. Mater. Interfaces*, 2023, **15**, 11662–11669.
28 E. L. Tyson, M. S. Ament and T. P. Yoon, *J. Org. Chem.*, 2013, **78**, 2046–2050.
29 V. T. Bhat, P. A. Duspara, S. Seo, N. S. B. Abu Bakar and M. F. Greaney, *Chem. Commun.*, 2015, **51**, 4383–4385.

30 Y. Li, J. Cai, M. Hao and Z. Li, *Green Chem.*, 2019, **21**, 2345–2351.
31 Z. Meng, Y. Ma, B. Chen, Y. Li, H. Ma, B. Zhu and F. Dong, *J. Colloid Interface Sci.*, 2024, **664**, 433–443.
32 G. Kumar, C.-R. Chen, B.-H. Chen, J.-W. Chen and M. H. Huang, *J. Mater. Chem. C*, 2022, **10**, 12125–12131.
33 J. Ma, C. Wang and H. He, *Appl. Catal. B: Environ.*, 2016, **184**, 28–34.